



HAL
open science

Inertia-dominated coiling instabilities of power-law fluids

Anselmo Pereira, Elie Hachem, Rudy Valette

► **To cite this version:**

Anselmo Pereira, Elie Hachem, Rudy Valette. Inertia-dominated coiling instabilities of power-law fluids. *Journal of Non-Newtonian Fluid Mechanics*, 2020, 282, pp.104321. 10.1016/j.jnnfm.2020.104321 . hal-03101983

HAL Id: hal-03101983

<https://minesparis-psl.hal.science/hal-03101983>

Submitted on 22 Aug 2022

HAL is a multi-disciplinary open access archive for the deposit and dissemination of scientific research documents, whether they are published or not. The documents may come from teaching and research institutions in France or abroad, or from public or private research centers.

L'archive ouverte pluridisciplinaire **HAL**, est destinée au dépôt et à la diffusion de documents scientifiques de niveau recherche, publiés ou non, émanant des établissements d'enseignement et de recherche français ou étrangers, des laboratoires publics ou privés.



Distributed under a Creative Commons Attribution - NonCommercial 4.0 International License

Inertia-dominated coiling instabilities of power-law fluids

Anselmo Pereira ^a, Elie Hachem ^a, Rudy Valette ^a

^a*MINES ParisTech, PSL Research University, Centre de Mise en Forme des Matériaux (CEMEF), CNRS UMR 7635, CS 10207 rue Claude Daunesse, 06904 Sophia-Antipolis, France.*

Abstract

In this note, we investigate through scaling laws and direct numerical simulations the development of inertia-dominated coiling instabilities in power-law fluids. Our numerical results are based on an adaptive variational multi-scale method for multiphase flows. In short, when inertia is balanced by viscous forces in the coil, both the coiling frequency and the coil radius are given by a power-law function of both the Reynolds number, and the flow behaviour index.

Key words: buckling instability, power-law fluid, compression, direct numerical simulation

Email addresses: anselmo.soeiro_pereira@mines-paristech.fr (Anselmo Pereira), elie.hachem@mines-paristech.fr (Elie Hachem), rudy.valette@mines-paristech.fr (Rudy Valette).

Preprint submitted to Journal of Non-Newtonian Fluid Mechanics July 2019

1 Introduction

The coiling instability represents one of most fascinating phenomena in fluid mechanics, being typically observed when free liquid filaments and/or jets are exposed to compression stresses (Barnes and Woodcock, 1958). Since the energy related to the coiling deformation becomes smaller than the cost of compression (Taylor, 1969; Cruickshank, 1988; Yarin and Tchavdarov, 1996; Mahadevan et al., 1998, 2000), slender viscous fluid filaments tend to buckle, beyond a critical axial load. For small Newtonian fluid filaments compressed at a very small Reynolds number (negligible inertial force), for instance, the folding deformation emerges from a competition between geometrical, surface tension and viscous effects (Le Merrer et al., 2012). In addition, Newtonian viscous jet columns can bend, twist and stretch when hitting a surface or a substrate at higher Reynolds numbers, following the balance between viscous, gravitational, and inertial forces (Ribe, 2003; Ribe et al., 2006, 2012). Such instabilities are observed in a variety of contexts, which includes glass plate fabrication (Pilkington, 1969), polymer processing (Pearson, 1985), and folding of geological structures (Griffiths and Turner, 1988; Johnson and Fletcher, 1994).

In industry, the coiling instability represents a major source of irregularities for container-filling processes related to non-Newtonian fluids. Typically, during these processes, the superposition of several coils, consecutively formed as a result of the fluid filament compression, originates a helical fluid column, the centre of which is filled with air. Later on, this column eventually collapses, entraining a significant amount of air towards the fluid substrate and

compromising the quality of the final product¹. Hence, understanding and controlling the coiling instabilities when dealing with this kind of processes is crucial. Despite some recent works concerning these instabilities in Newtonian contexts (Le Merrer et al., 2012; Habibi et al., 2014; Ribe, 2017) many aspects of the problem remain unclear, such as the effects of non-Newtonian signatures (pseudoplasticity, dilatancy, thixotropy, yield stress etc.)² on them (Tomé et al., 2019; Pereira et al., 2019).

In the present work, we study the inertia-dominated coiling process of slender pseudoplastic, Newtonian and dilatant fluid filaments, of which viscosity is given by a power-law constitutive equation (Ostwald, 1925; Bird et al., 1987). In other words, we aim in this note to highlight both shear-thinning and shear-thickening effects on inertia-dominated coiling instabilities. The coiling development in time is carefully analysed thanks to an adaptive variational multi-scale method for two materials (air, non-Newtonian fluid), combined with a level-set function to provide a precise position of the phase interfaces. Both the coiling frequency and the coil radius are explored in the light of scaling laws. According to analyses, the inertia-dominated coiling dynamics of power-law fluids can be expressed as a function of the Reynolds number.

The organization of the paper is as follows. The description of the physi-

¹ **movie-1**: experimental movie showing the collapse of a 330 Pas silicone oil spire column is shown in a supplemental movie (also available on <https://anselmopereira.net/videos/>).

² **movie-2**: experimental movie showing coiling instabilities in a non-Newtonian suspension of small glass spheres (diameter $\approx 200 \mu\text{m}$) dispersed in a 330 Pas silicone oil matrix (volume fraction $\approx 55\%$) is provided to illustrate Section 1 (also available on <https://anselmopereira.net/videos/>).

cal formulation and numerical method is presented in Section 2. Our main results are discussed in Section 3, where the inertia-dominated coiling of non-Newtonian fluid filaments is analysed. Finally, conclusions are drawn in the closing section.

2 Physical Formulation and Numerical Method

As illustrated in Fig. 1, we consider in this note coiling instabilities developed in a viscous power-law filament (yellow part) surrounded by air (blue part). The non-Newtonian fluid of density ρ and viscosity η leaves a hole of radius r_0 with a velocity $U_{z,0}$ and falls onto a plate (Figs. 1*a* and 1*b*) on which it forms a helical coil of radius R that rotates with an angular frequency Ω around a vertical axis z (Figs. 1*c* and 1*d*). The fall height is the distance H from the upper hole to the first point of contact of the free portion of the power-law filament with the pile of fluid accumulated on the plate. The radius of the trailing part of the filament, called tail, generally varies downward, and its value in the coil is r_1 . At the steady state configuration the filament develops an axial velocity $U_{z,1} = Q/(\pi r_1^2)$ at the contact point, where Q denotes the volume flow rate (a supplemental movie illustrating this process is available)³.

The computational approach used to simulate the coiling process is based on a general solver (CIMLIB-CFD, a parallel, finite element library; Coupez and Hachem, 2013) which takes into account the rheological behaviour of each fluid as well as surface tension effects (Valette et al., 2019; Pereira et al., 2019).

³ **movie-3:** numerical results showing the formation of ten consecutive spires for a Newtonian jet (300 Pas; 1000 Kg/m³) that leaves a hole at $U_{z,0}$ 1.5 m/s. This movie is also available on <https://anselmopereira.net/videos/>.

More precisely, the Cauchy stress tensor $\boldsymbol{\sigma}_c$ is defined as

$$\boldsymbol{\sigma}_c = -p\mathbf{I} + \boldsymbol{\tau}, \quad (1)$$

where, p is the pressure, \mathbf{I} denotes the identity tensor and $\boldsymbol{\tau}$ the *extra stress tensor*. The extra stress tensor is given by

$$\boldsymbol{\tau} = 2\eta\mathbf{D}(\mathbf{u}), \quad (2)$$

$\mathbf{D}(\mathbf{u})$ representing the strain rate tensor and \mathbf{u} the velocity vector. The effective viscosity η is computed by using the power-law constitutive model. The latter includes the Papanastasiou regularization (Papanastasiou, 1987):

$$\eta = k\dot{\gamma}^{m-1} \left(1 - e^{-\dot{\gamma}/n}\right)^{1-m}, \quad (3)$$

where k is the flow consistency index, m denotes the flow behaviour index, $\dot{\gamma}$ represents the second invariant of the strain rate tensor (Bird et al., 1987) and n is the Papanastasiou coefficient that allows to bound the value of the effective viscosity for vanishing $\dot{\gamma}$. In addition, the momentum equation reads:

$$\rho \left(\frac{\partial \mathbf{u}}{\partial t} + \mathbf{u} \cdot \nabla \mathbf{u} - \mathbf{g} \right) = -\nabla p + \nabla \cdot \boldsymbol{\tau} + \mathbf{f}_{st}, \quad (4)$$

in which ρ , ∇ , \mathbf{g} , $\nabla \cdot$ and \mathbf{f}_{st} are, respectively, the fluid density, the gradient operator, the gravity vector, the divergence operator, and a capillary term related to the surface tension force. Because surface tension has a relatively minor effect on the coiling frequency for typical experimental fluids (between 1% and 20%, as pointed out by Ribe et al. (2012)), we neglect it in the following discussion, i.e. \mathbf{f}_{st} is null.

Our numerical methods are based on a Variational Multi-Scale (VMS) approach combined with anisotropic mesh adaptation with highly stretched el-

ements (black lines in Fig. 1), as presented by Riber et al. (2016). In order to capture the fluid/air, fluid/pistons and pistons/air interfaces as a function of time, t , a level-set method, which enables the localization and the capturing of interfaces has been used (Hachem et al., 2016). Velocity and pressure fields are primitive unknowns that are computed using a unified framework, where all fluids occupy a single computational mesh, by simply mixing the different fluid properties (viscosity, density, etc.) using smoothed Heaviside functions (built from each level-set function) to take property discontinuities into consideration.

The numerical configuration taken into account in this work is illustrated in Fig. 1, where the mesh is depicted, adapted around each interface (the number of mesh elements per unit height N/H is equal to 2500000; a sensitivity analysis is presented in Appendix). The corresponding zero-isovalues for the level-set function are also shown. The upper hole radius r_0 is kept constant. Nevertheless, a wide range of filament fluid properties, initial filament velocity, and fall height is considered: $1000 < \rho < 5000 \text{ kg/m}^3$; $0.7 \leq m \leq 1.3$; $(O)10^0 < k < (O)10^2 \text{ Pa}\cdot\text{s}^m$; $0.4 < H < 1\text{m}$; and $(O)10^{-1} < U_{z,0} < (O)10^0 \text{ m/s}$. Additionally, both the air viscosity η_{air} and the air density ρ_{air} are constant and respectively equal to $10^{-5} \text{ Pa}\cdot\text{s}$ and 1 kg/m^3 . The Papanastasiou coefficient is kept constant $n = 10^{-5}$ (for more details, see Appendix). Lastly, initial and boundary conditions for the flow equations are, respectively, initial velocity $U_{z,0}$ at the upper hole, and zero normal stress in the air domain.

3 Results and Discussion

As previously reported by Ribe et al. (2012), in viscous fluids, coiling instabilities can develop basically four different regimes, each of them corresponding to a different balance among the viscous, gravitational, and inertial forces that controls the motion of the filament. In the first regime, which is called *viscous*, the fall height is very small and consequently the coiling is so slow that both gravity and inertia are negligible when compared with viscous forces. The second regime, the *gravitational* one, takes place when gravity balances viscous forces in the entire filament, while the third one, called *inertio-gravitational*, is observed when inertia becomes relevant and is balance by gravity and the viscous forces within the tail (dominated by stretching). The last regime appears when the gravity becomes negligible relative to inertia and consequently the latter is balanced by viscous forces in the coils (in which the deformation is dominated by bending). This regime is called *inertial* and, as will be shown, the following results are related to it.

Figure 2 illustrates the time evolution of the buckling process for two power-law fluids, as well as the formation of their first three coils. The initial fluid vertical velocity $U_{z,0}$ (1.75 m/s), the flow consistency k (300 Pa s^{*m*}), and the fluid density (1000 kg/m³) are kept fixed, while two flow behaviour indexes are considered: $m = 0.7$ (Fig. 2*a*; pseudo-plastic or *shear-thinning* fluid in blue) and $m = 1.3$ (Fig. 2*b*; dilatant or *shear-thickening* fluid in red). Following the jet descent and its subsequent impact on the bottom part of the container (leftmost image in Fig. 2), the power-law filaments initially tend to fold. Clearly, a more pronounced filament deflection is observed for the shear-thickening fluid (red fluid in Fig. 2*b*). This material develops higher viscosity values within the buckled regions, as indicated by the contours displayed in

the folding plane at $t = 0.33\text{s}$ (see the viscosity contours on the left side of the filaments; its right side represents zero iso-values of the level-set function). A fluid column is then formed by the superposition on successive folded fluid layers ($t = 0.43\text{s}$), which later on collapses ($t \approx 0.53\text{s}$) perturbing the jet and, finally, triggering the coiling process (Ribe et al., 2012). Helical coils of radius R that rotate with an angular frequency Ω are then formed ($t > 0.63\text{s}$; see also supplemental movie-4)⁴. During the coiling formation, the tail remains perfectly vertical for the $m = 0.7$ case (which is an important signature of the inertial regime), while almost half of it appears perturbed for the $m = 1.3$ case.

Because of the development of larger viscous forces within the twisted parts of the shear-thickening filament, the latter exhibits a more pronounced resistance to deformation and hence a bigger coil diameter R than the shear-thinning fluid, as illustrated by Fig. 3, where the contours represent both the air and the viscous filament viscosity in the centre $x - y$ plane⁵. However, since the energetic cost of compression at $m = 0.7$ is relatively smaller, the downward part of the shear-thinning jet tends to swell as a result of the compression stresses. In consequence, its radius r_1 becomes larger than that observed in the shear-thickening fluid (the swelling of the downward part of the shear-thinning jet is indicated by the black arrows in Fig. 2).

⁴ **movie-4**: supplemental movie comparing coiling instabilities of power-law fluids of $m = 0.9$ and $m = 1.1$ is provided (also available on <https://anselmopereira.net/videos/>).

⁵ Since the coils can eventually exhibit an elliptical shape as the Reynolds number decreases and, consequently, the coiling dynamics approaches the boundaries of the inertio-gravitational regime (Fig. 3*b*), in this note we define $2R$ as the maximum distance between the interfaces of a single coil, as indicated in Fig. 3.

It is important to emphasise that, as the inertial forces are attenuated with the increase of m , the coiling dynamics approaches the boundaries of the inertio-gravitational regime and, thus, elliptical coils are eventually formed, such as that displayed in Fig. 3(b) (even though inertia is still dominant for the $m = 1.3$ case, as shown in the following lines of this note).

Viscous dissipation W , kinetic energy KE , and gravitational potential energy G rate terms are displayed in Fig. 4 as a function of time, t , for the two power-law fluids mentioned above: (a) $m = 0.7$; (b) $m = 1.3$. These terms are respectively defined as

$$W = \int_V \eta \dot{\gamma}^2 dV \quad (\text{viscous dissipation rate, J/s}), \quad (5)$$

$$KE = \frac{1}{2} \frac{\partial \int_V \rho \| \mathbf{u} \|^2 dV}{\partial t} \quad (\text{kinetic energy rate, J/s}), \quad (6)$$

and

$$G = \frac{\partial \int_V \rho g h dV}{\partial t} \quad (\text{gravitational potential energy rate, J/s}), \quad (7)$$

V being the volume of the power-law fluid. Actually, the energy variations are primarily located at the coil being formed.

The pink, gray and white regions in Fig. 4 indicate the formation of a single coil. The length of this regions (which is denoted by the black arrows) represents the time required to form a coil, Δt ($\Delta t = 0.15\text{s}$ at $m = 0.7$; and $\Delta t = 0.21\text{s}$ at $m = 1.3$). Therefore, during the time interval of 0.5s considered in Fig. 4, three consecutive coils are completely formed at $m = 0.7$ (blue structures), while only two of them are formed at $m = 1.3$ (red structures).

Regarding the energy rate terms Π (where Π can represent G , W or KE), we easily note that, for both materials shown in Fig.4, G (gray circles/line) is practically negligible when compared with W (blue triangles/line) and KE

(red diamonds/line). In addition, more pronounced viscous dissipation rate values are observed for the shear-thickening fluid (Fig.4b), which is related to its viscous resistance to deformations, as discussed previously. Interestingly, for both cases, W and KE appear as being strongly correlated, i.e. $KE \sim -W$. This leads us to conclude that the kinetic energy of the filament is primarily dissipated by viscous effects during the coil formation (the inertia is balanced by viscous forces in the coil; see also Mahadevan et al., 1998, 2000). Furthermore, these results allow us to stress some coiling instability scaling laws based on a global energetic approach, as shown in the following lines.

Globally, the kinetic energy variation during the formation of a single coil, $KE_{1,c}$, can be expressed as

$$KE_{1,c} = \frac{\Delta E_{1,c}}{\Delta t} \sim \frac{m_{1,c} U_{1,z}^2}{\Omega}, \quad (8)$$

where $E_{1,c}$ denotes the kinetic energy of a single coil, and Ω represents the coiling frequency. The mass of a coil, $m_{1,c}$, is $m_{1,c} \sim \rho r_1^2 R$. Thus,

$$KE_{1,c} \sim \rho r_1^2 R U_{1,z}^2 \Omega. \quad (9)$$

However, the velocity $U_{z,1}$ can be expressed as a function of the flow rate Q : $U_{z,1} \sim Q/r_1^2$. Consequently, $KE_{1,c}$ takes the form

$$KE_{1,c} \sim \frac{\rho R Q^2 \Omega}{r_1^2}. \quad (10)$$

In addition, the variations of viscous dissipation energy during the formation a coil, $W_{1,c}$, is defined as

$$W_{1,c} = \int_{V_{1,c}} \eta \dot{\gamma}_{1,c}^2 dV_{1,c} \sim \int_0^{r_1} k \dot{\gamma}_{1,c}^{m-1} \dot{\gamma}_{1,c}^2 R r_1 dr_1, \quad (11)$$

in which $V_{1,c}$ denotes the volume of the coil, and $\dot{\gamma}_{1,c}$ represents the characteristic coiling strain rate. In order to calculate $\dot{\gamma}_{1,c}$, we take into account both

folding and rotation deformations. The former is given by $2\pi r_1/2\pi R$, and the latter is computed as $b2\pi r_1/2\pi R$ (b denoting the twist percentage, $b > 0$).

Therefore,

$$\dot{\gamma}_{1,c} = \frac{\Delta\gamma_{1,c}}{\Delta t} = \frac{\left[\left(\frac{2\pi r_1}{2\pi R}\right) + \left(\frac{a2\pi r_1}{2\pi R}\right)\right]}{\left(\frac{2\pi}{\Omega}\right)} \Rightarrow \left[\underbrace{\left(\frac{2\pi r_1}{2\pi R}\right)}_{\text{folding}} + \underbrace{\left(\frac{a2\pi r_1}{2\pi R}\right)}_{\text{torsion}} \right] \left(\frac{\Omega}{2\pi}\right), \quad (12)$$

or simply

$$\dot{\gamma}_{1,c} \sim \frac{r\Omega}{R}. \quad (13)$$

An expression for $W_{1,c}$ is then found by replacing Eq. 13 in Eq. 11:

$$W_{1,c} \sim \left(\frac{1}{m+3}\right) \frac{r_1^{m+3}\Omega^{m+1}}{R^m}. \quad (14)$$

Assuming that $KE_{1,c} \sim W_{1,c}$ (as indicated in Fig. 4; Eq. 10 = Eq. 14), and that $R \sim U_{z,1}/\Omega \sim Q/(\Omega r_1^2)$, we find:

$$\Omega \sim \left(\frac{\rho}{k} \frac{Q^{m+3}}{r_1^{3m+7}}\right)^{\frac{1}{2m+1}}. \quad (15)$$

Since $R \sim Q/(\Omega r_1^2)$, we can replace Ω in this equation by the expression given above and rewrite the coil radius as

$$R \sim \left(\frac{k}{\rho} \frac{r_1^{5-m}}{Q^{2-m}}\right)^{\frac{1}{2m+1}}. \quad (16)$$

For a Newtonian fluid, $m = 1$ and then $\Omega \sim \left(\frac{\rho}{k} \frac{Q^4}{r_1^{10}}\right)^{\frac{1}{3}}$ and $R \sim \left(\frac{k}{\rho} \frac{r_1^4}{Q}\right)^{\frac{1}{3}}$, as previously reported by Mahadevan et al. (1998, 2000). Finally, rewriting both Eqs. 15 and 16 as a function of the Reynolds number defined as $\text{Re} = \left(\frac{8m}{6m+2}\right) \left(\frac{\rho U_{z,1}^{2-m} 2^m r_1^m}{k}\right)$ (see Metzner and Reed, 1955),

$$\Omega \frac{r_1}{U_{z,1}} \sim \text{Re}^{\frac{1}{2m+1}} \quad \text{and} \quad \frac{R}{r_1} \sim \text{Re}^{\frac{-1}{2m+1}}, \quad (17)$$

Equations 17 are in excellent agreement with all the 200 flow cases concerning inertia-dominated coiling instabilities of power-law fluids explored in the

present note. Some of these cases (45 of them) are displayed in Figs. 5(*a*) and 5(*b*), in which Ω and R (made dimensionless by r_1 and $U_{z,1}/r_1$) appear as a linear function of $\text{Re}^{\frac{-1}{2m+1}}$ and $\text{Re}^{\frac{1}{2m+1}}$, respectively (both R and Ω are mean values calculated by taken into account over 20 consecutive coils). In other words, $R/r_1 = (1/a)\text{Re}^{\frac{-1}{2m+1}}$ and $\Omega r_1/U_{z,1} = a\text{Re}^{\frac{1}{2m+1}}$, where a is a prefactor related to each power-law fluid. Clearly, at a fixed $\text{Re}^{\frac{1}{2m+1}}$, the increase of m leads to a higher dimensionless coiling frequency, as well as a smaller dimensionless coil radius. Furthermore, when $\text{Re}^{\frac{-1}{2m+1}} \rightarrow 1$, R becomes comparable to r_1 ($R \approx r_1$) and, then, coiling ceases (as shown in supplemental movie-5; this movie is also available on <https://anselmopereira.net/videos/>)⁶. Finally, as displayed in Figs. 5(*c*) and 5(*d*), our points collapse onto a single curve when both the dimensionless coil radius and coiling frequency are redefined as aR/r_1 and $(\Omega/a)/(U_{z,1}/r_1)$.

4 Concluding Remarks

We have presented in this note some new results in an attempt to highlight inertia-dominated coiling instabilities of power-law fluid filaments. Our analyses were conducted through scaling laws and direct numerical simulations of multiphase flows (power-law fluid/air). A level-set function was used to provide a precise position of the fluid interfaces.

⁶ **movie-5:** numerical results showing that the coiling process ceases for power-law jet of $m = 0.7$, $k = 300\text{Pas}^m$, and $\rho = 1000 \text{ Kg/m}^3$ at higher $\text{Re}^{\frac{-1}{2m+1}}$. This effect is expressed through the increase of $U_{z,0}$. At $U_{z,0} = 0.75 \text{ m/s}$ (*a*), coiling instabilities develop with a small R (close to r_1). However, at $U_{z,0} = 1.25 \text{ m/s}$, these instabilities tend to vanish (*b*), being finally suppressed at $U_{z,0} = 1.75 \text{ m/s}$ (*c*).

In short, when inertia is balanced by viscous forces in the coil (inertia-dominated coiling), both the coiling frequency, Ω , and the coil radius, R (made dimensionless by $U_{z,1}/r_1$ and r_1 , respectively) appear as a function of both the Reynolds number, Re , and the flow consistency index, m . More specifically, $\Omega r_1/U_{z,1} = a\text{Re}^{\frac{1}{2m+1}}$, while $R/r_1 = (1/a)\text{Re}^{\frac{-1}{2m+1}}$ (in which a is a prefactor related to each power-law fluid). For instance, for a Newtonian fluid, $m = 1$ and, consequently, $\Omega r_1/U_{z,1} \sim \text{Re}^{\frac{1}{3}}$ and $R/r_1 \sim \text{Re}^{-\frac{1}{3}}$, as previously reported by Mahadevan et al. (1998, 2000).

It would be interesting to consider in future works supplemental coiling regimes, such as the viscous, and the gravitational ones, as well as the effects of other non-Newtonian entities (such as the yield-stress) on them.

Acknowledgements

We would like to express our sincere gratitude to PSL Research University for their support under the program ‘Investissements d’Avenir’ launched by the French Government and implemented by the French National Research Agency (ANR) with the reference ANR-10-IDEX-0001-02 PSL.

Appendix: sensitivity analysis

As exposed in Section 2, our numerical analyses are based on an adaptive stabilized finite element framework able to compute efficiently free surface flows of highly non-Newtonian materials. We choose to focus on the power-law model. Momentum and mass equations are solved by using the Variational MultiScale method coupled with a regularization technique and anisotropic mesh adaptation. A convective self-reinitialization Level-Set method is used

to describe the interface evolution. Detailed descriptions and validations of this framework for different flow cases (such as the stretching and the compression of non-Newtonian filaments) can be found in Coupez and Hachem (2013); Hachem et al. (2016); Riber et al. (2016); Valette et al. (2019); Pereira et al. (2019).

Regarding the numerical simulations presented in this note, Fig. 6 shows a sensitivity study for the non-Newtonian fluids considered in Fig. 2: $\rho = 1000$ kg/m³; $k = 300$ Pa·s^{*m*}; $m = 0.7$ (blue triangles); and $\rho = 1000$ kg/m³; $k = 300$ Pa·s^{*m*}; $m = 1.3$ (red diamonds).

Computations linking both R/r_1 and $\Omega r_1/U_{z,1}$ with the number of mesh elements per unit height (N/H) are shown in Figs. 6(a) and Figs. 6(b), respectively. Each curve is constructed by keeping the channel-based Reynolds number fixed, $\text{Re}_0 = \left(\frac{8m}{6m+2}\right) \left(\frac{\rho U_{z,0}^{2-m} 2^m r_0^m}{k}\right)$ (we do not use here the impact-based Reynolds number presented in the main part of this note because the impact parameters R , r_1 , and $U_{z,1}$ can be affected by small values of N , as exposed in the following lines). Clearly, both R/r_1 and $\Omega r_1/U_{z,1}$ become mesh independent for $N/H > 1750000$ m⁻¹ (gray regions).

A sensitivity analysis regarding the impact of the Papanastasiou coefficient n on R/r_1 and $\Omega r_1/U_{z,1}$ is presented in Figs. 6(c) and 6(d), respectively, for $N/H = 2500000$. Since the inertia-dominated coiling cases discussed here are related to relatively high strain rate levels ($(O)10^2 < u_1/r_1 < (O)10^3$ s⁻¹), no effects of n on R/r_1 and $\Omega r_1/U_{z,1}$ are observed for $10^{-3} \leq n \leq 10^{-5}$. In other words, the employed Papanastasiou normalization has no effect on the coiling mechanism, and exclusively bounds viscosity values far from the centre spire column, where the local strain rate can eventually become close to zero.

References

- Barnes, G., Woodcock, R., 1958. Liquid rope-coil effect. *American Journal of Physics* 26, 205–209.
- Bird, R.B., Armstrong, R.C., Hassager, O., 1987. Dynamics of polymeric liquids. Wiley-Interscience, New York 2nd edition, 172–173.
- Coupez, T., Hachem, E., 2013. Solution of high-Reynolds incompressible flow with stabilized finite element and adaptive anisotropic meshing. *Computer Methods in Applied Mechanics and Engineering* 267, 65–85.
- Cruickshank, J.O., 1988. Low-Reynolds-number instabilities in stagnating jet flows. *Journal of Fluid Mechanics* 193, 111–127.
- Griffiths, R.W., Turner, J.S., 1988. Folding of viscous plumes impinging on a density or viscosity interface. *Geophysical Journal International* 95, 397–419.
- Habibi, M., Hosseini, S.H., Khatami, M.H., Ribe, N.M., 2014. Liquid supercoiling. *Physics of Fluids* 26, 024101–1–024101–11.
- Hachem, E., Khalloufi, M., Bruchon, J., Valette, R., Mesri, Y., 2016. Unified adaptive variational multiscale method for two phase compressible and incompressible flows. *Computer Methods in Applied Mechanics and Engineering* 308, 238–255.
- Johnson, A.M., Fletcher, R.C., 1994. Folding of viscous layers: Mechanical analysis and interpretation of structures in deformed rock. Columbia University, New York .
- Le Merrer, M., Quéré, D., Clanet, C., 2012. Buckling of viscous filaments of a fluid under compression stresses. *Physical Review Letters* 109, 064502.
- Mahadevan, L., Ryu, W.S., Samuel, A.D.T., 1998. Fluid 'rope trick' investigated. *Nature* 392, 140.

- Mahadevan, L., Ryu, W.S., Samuel, A.D.T., 2000. Correction: Fluid 'rope trick' investigated. *Nature* 403, 502.
- Metzner, A.B., Reed, J.C., 1955. Flow of non-Newtonian fluids-correlation of the laminar, transition, and turbulent-flow regions. *AIChE Journal* 1, 434–440.
- Ostwald, W., 1925. Ueber die geschwindigkeitsfunktion der viskosität disperser systeme. *Kolloid-Z* 36, 99–117.
- Papanastasiou, T., 1987. Flows of materials with yield. *Journal of Rheology* 31, 385–404.
- Pearson, J., 1985. *Mechanics of polymer processing*. Elsevier, Amsterdam .
- Pereira, A., Larcher, A., Hachem, E., Valette, R., 2019. Capillary, viscous, and geometrical effects on the buckling of power-law fluid filaments under compression stresses. *Computers and Fluids* 190, 514–519.
- Pilkington, L.A.B., 1969. Review lecture: The float glass process. *Transport Phenomena and Fluid Mechanics*, *AIChE Journal* 314, 1–25.
- Ribe, N.M., 2003. Periodic folding of viscous sheets. *Physical Review E* 68, 036305–1–036305–6.
- Ribe, N.M., 2017. Liquid rope coiling: a synoptic view. *Journal of Fluid Mechanics* 812, R2.
- Ribe, N.M., Habibi, M., Bonn, D., 2012. Liquid rope coiling. *Annual Review of Fluid Mechanics* 44, 249–266.
- Ribe, N.M., Huppert, H.E., Hallworth, M.A., Habibi, M., Bonn, D., 2006. Multiple coexisting states of liquid rope coiling. *Journal of Fluid Mechanics* 555, 275–297.
- Riber, S., Valette, R., Mesri, Y., Hachem, E., 2016. Adaptive variational multiscale method for Bingham flows. *Computers and Fluids* 138, 51–60.
- Taylor, G.I., 1969. *Proceedings of the Twelfth International Congress of Ap-*

- plied Mechanics, Stanford, 1968 Springer-Verlag, Berlin, 382.
- Tomé, M.F., Araujo, M.T., Evans, J., Mckee, S., 2019. Numerical solution of the giesekus model for incompressible free surface flows without solvent viscosity. *Journal of Non-Newtonian Fluid Mechanics* 263, 104–119.
- Valette, R., Hachem, E., Khalloufi, M., Pereira, A.S., Mackley, M.R., Butler, S.A., 2019. The effect of viscosity, yield stress, and surface tension on the deformation and breakup profiles of fluid filaments stretched at very high velocities. *Journal of Non-Newtonian Fluid Mechanics* 263, 130–139.
- Yarin, A.L., Tchavdarov, B.M., 1996. Onset of folding in plane liquid films. *Journal of Fluid Mechanics* 307, 85–99.

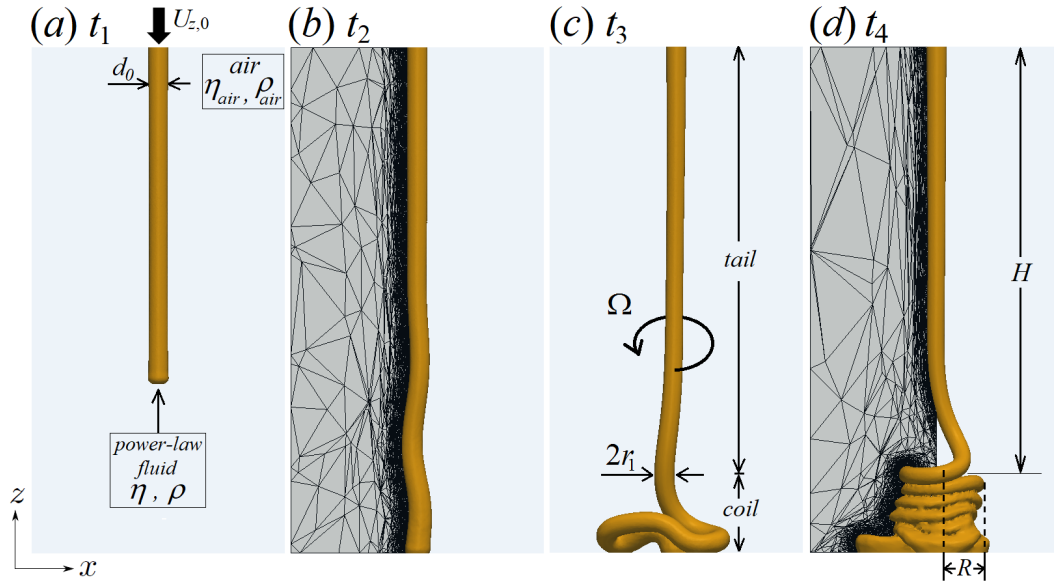


Fig. 1. Time evolution ($t_1 \leq t \leq t_4$) of the buckling process of a power-law fluid filament. Yellow parts: zero iso-values of the fluid filament level-set function. Blue part: air. Left in (b) and (d): adapted mesh ($\approx 10^6$ elements) of the computational domain.

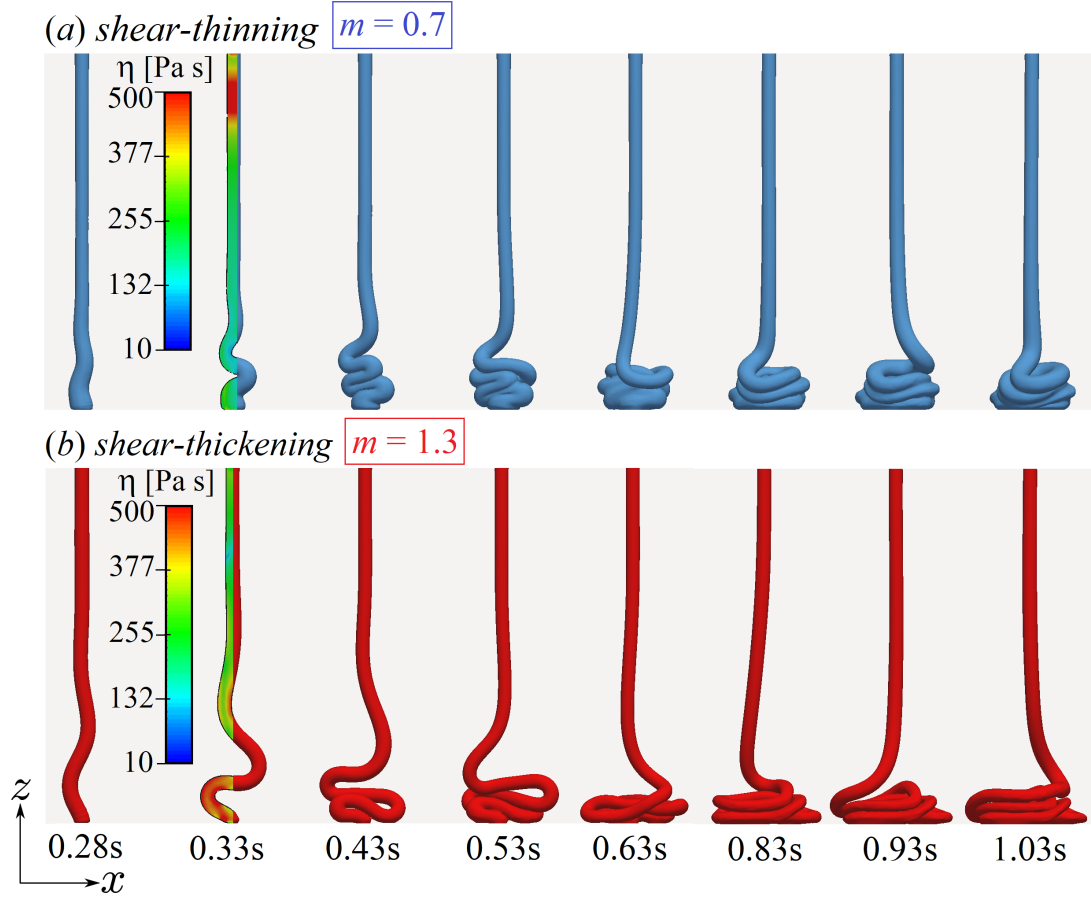


Fig. 2. Time evolution of the coiling process in two power-law fluids. The initial fluid vertical velocity $U_{z,0}$ (1.75 m/s), the flow consistency k ($300 \text{ Pa}\cdot\text{s}^m$), and the fluid density (1000 kg/m^3) are kept fixed, while two flow behaviour indexes are considered: $m = 0.7$ (a; fluid in blue) and $m = 1.3$ (b; fluid in red). Eight different instants are considered: $0.28 \leq t \leq 1.03\text{s}$.

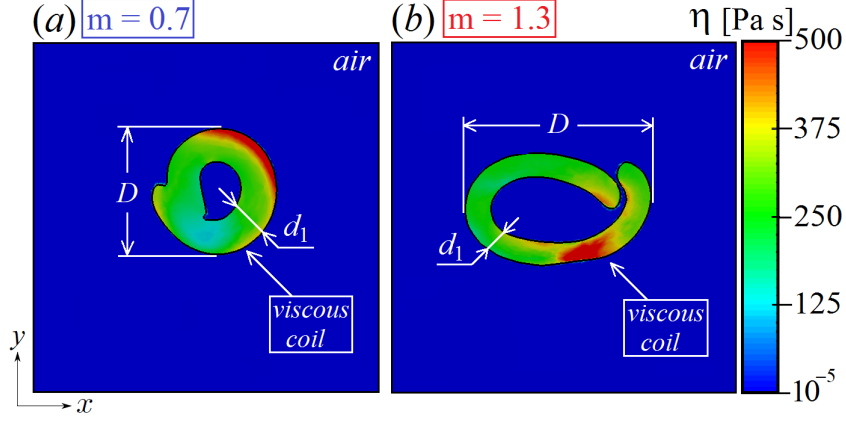


Fig. 3. Typical coil profiles of two power-law fluids together with viscosity contours in the horizontal $x - y$ plane: $m = 0.7$ (a) and $m = 1.3$ (b). The initial fluid vertical velocity $U_{z,0}$ (1.75 m/s), the flow consistency k (300 Pa·s m), and the fluid density ρ (1000 kg/m 3) are kept fixed.

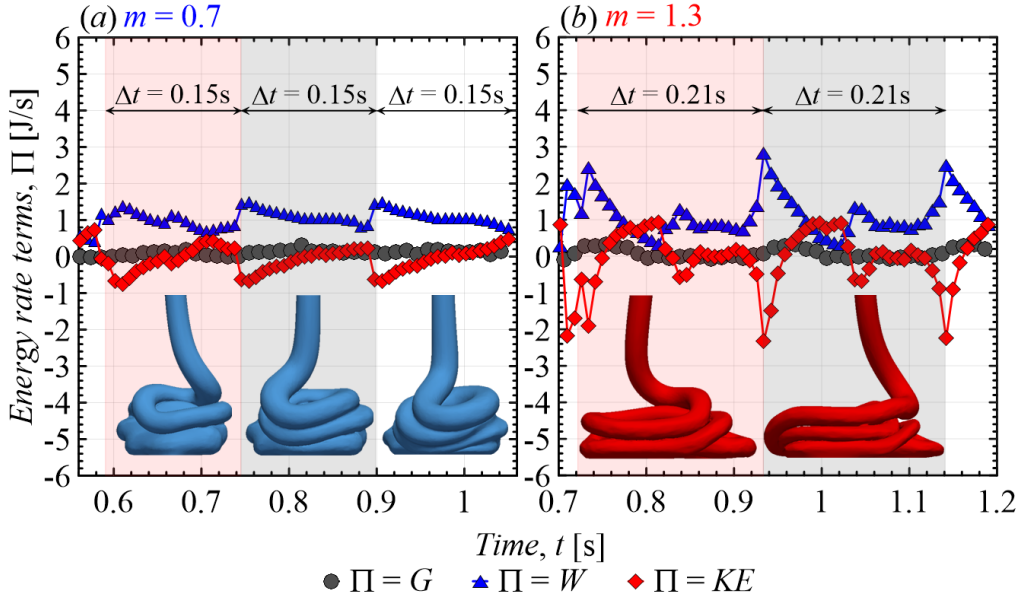


Fig. 4. Viscous dissipation W , kinetic energy KE , and gravitational potential energy G rate terms as a function of time, t , for the two power-law fluids: $m = 0.7$ (a) and $m = 1.3$ (b). The initial fluid vertical velocity $U_{z,0}$ (1.75 m/s), the flow consistency k (300 Pa·s m), and the fluid density ρ (1000 kg/m 3) are kept fixed.

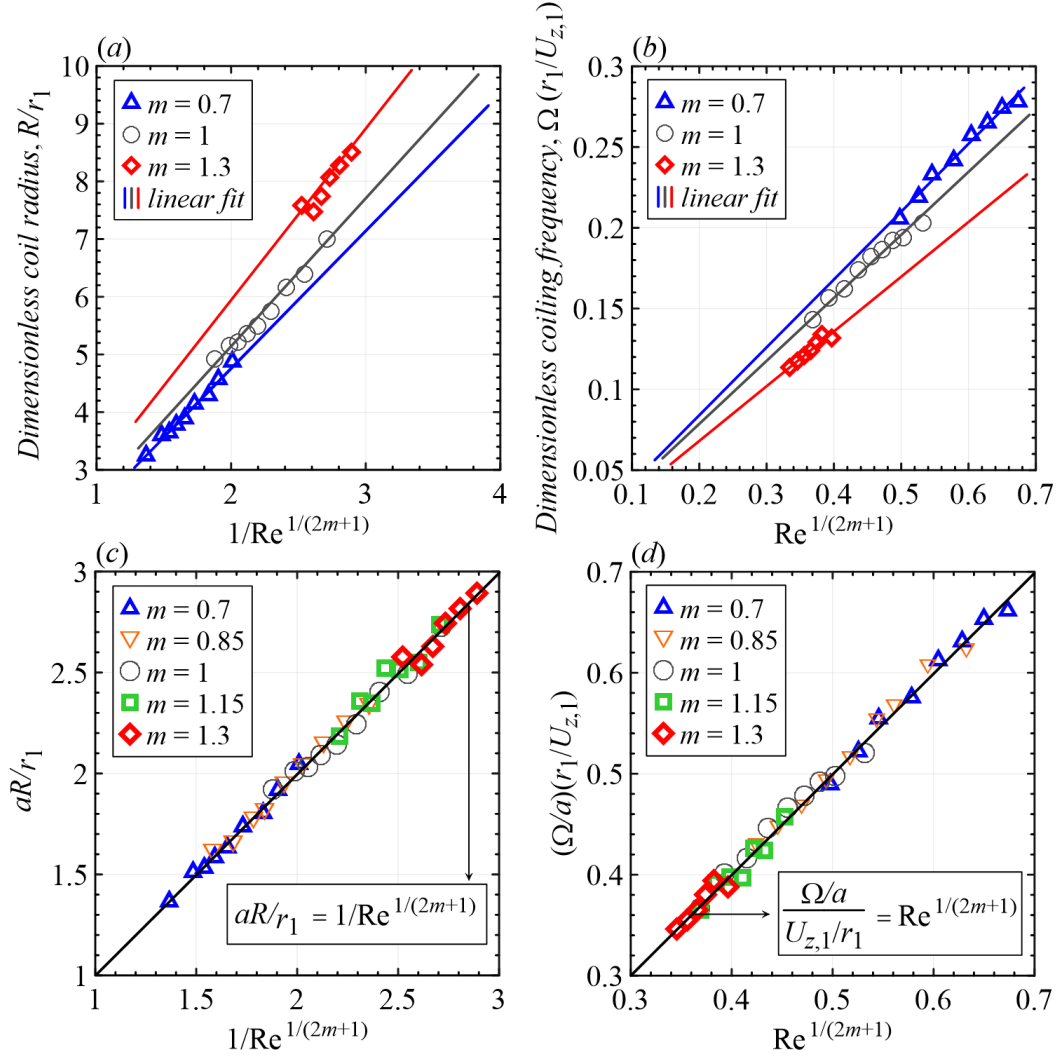


Fig. 5. Coil radius R (a/c) and coiling frequency Ω (b/d) made dimensionless by r_1 and $U_{z,1}/r_1$ appear as a linear function of $\text{Re}^{-\frac{1}{2m+1}}$ and $\text{Re}^{\frac{1}{2m+1}}$, respectively. Numerical results are denoted by symbols (each point representing a flow case), while scaling laws are represented by solid lines (a denoting their slopes).

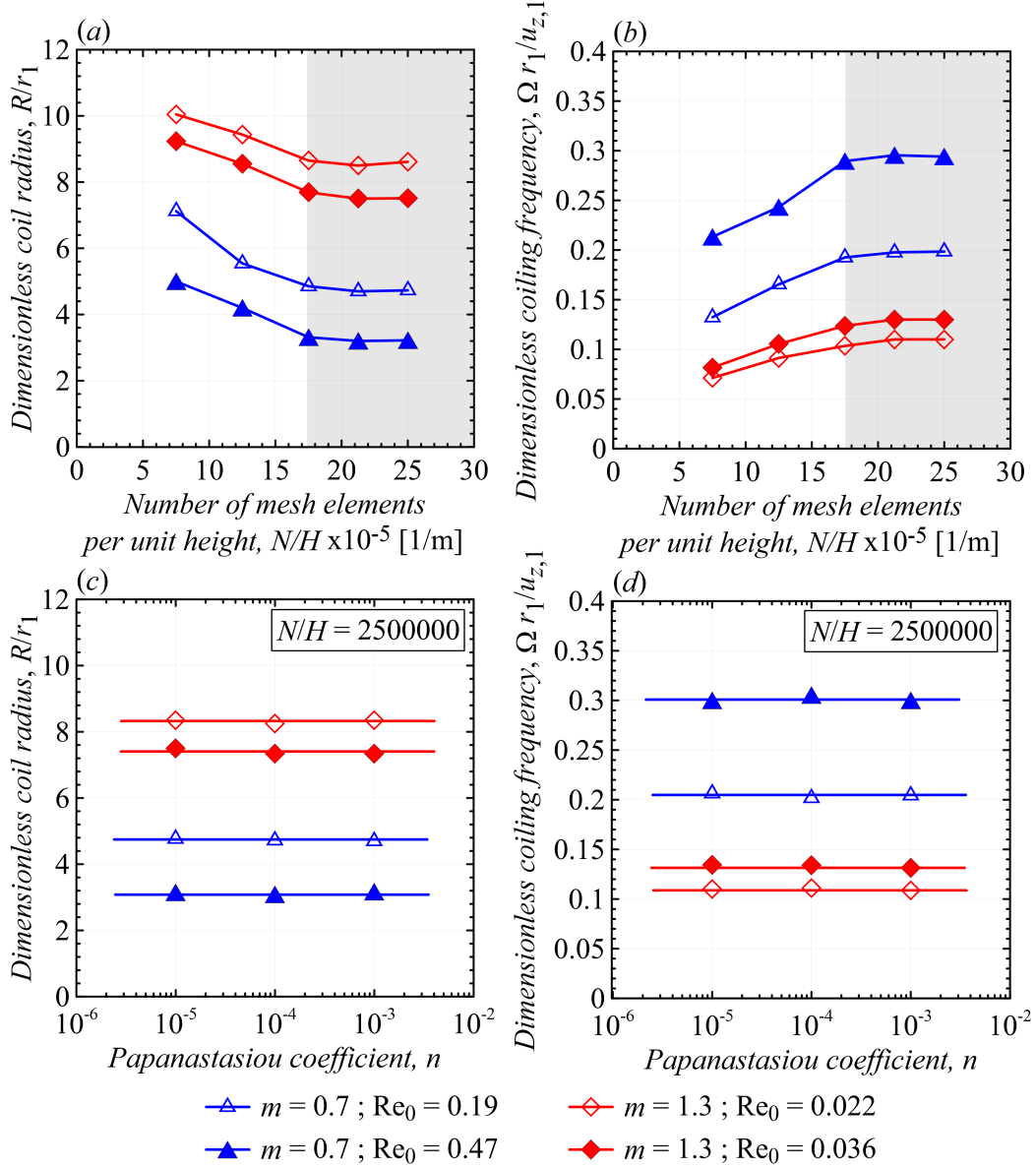


Fig. 6. Sensitivity study for the non-Newtonian fluids considered in Fig. 2: $\rho = 1000$ kg/m^3 ; $k = 300$ $\text{Pa}\cdot\text{s}^m$; $m = 0.7$ (blue triangles); and $\rho = 1000$ kg/m^3 ; $k = 300$ $\text{Pa}\cdot\text{s}^m$; $m = 1.3$ (red diamonds). Computations linking both R/r_1 and $\Omega r_1 / U_{z,1}$ with the number of mesh elements per unit height (N/H) are shown in (a) and (b), respectively. Each curve is constructed by keeping the channel-based Reynolds number fixed, $\text{Re}_0 = \left(\frac{8m}{6m+2}\right) \left(\frac{\rho U_{z,0}^{2-m} 2^m r_0^m}{k}\right)$. The impact of the Papanastasiou coefficient n on R/r_1 and $\Omega r_1 / U_{z,1}$ is presented in (c) and (d), respectively, for $N/H = 2500000$. Since the inertia-dominated coiling cases discussed here are related to relatively high strain rate levels ($u_1/r_1 > 100$ s^{-1}), no effects of n on R/r_1 and $\Omega r_1 / U_{z,1}$ are observed for $10^{-3} \leq n \leq 10^{-5}$.